Paper reference: K. Abbas, M. Puigt, G. Delmaire and G. Roussel, "Locally-Rank-One-Based Joint Unmixing and Demosaicing Methods for Snapshot Spectral Images. Part I: A Matrix-Completion Framework," in IEEE Transactions on Computational Imaging, vol. 10, pp. 848-862, 2024.

IEEE online version: `https://dx.doi.org/10.1109/TCI.2024.3402322`.

Locally-Rank-One-Based Joint Unmixing and Demosaicing Methods for Snapshot Spectral Images. Part I: a Matrix-Completion Framework

Kinan Abbas, *Student Member, IEEE,* Matthieu Puigt, *Member, IEEE,* Gilles Delmaire, and Gilles Roussel

***Abstract*—With the recent advancements in design and processing speed, a new snapshot mosaic imaging sensor architecture (SSI) has been successfully developed, holding the potential to transform the way dynamic scenes are captured using miniaturized platforms. However, SSI systems encounter a core trade-off concerning spatial and spectral resolution due to the assignment of individual spectral bands to each pixel. While the SSI camera manufacturer provides a pipeline to process such data, we propose in this paper to process the RAW SSI data directly. We show this strategy to be much more accurate than post-processing after the pipeline. In particular, in the first part of this paper, we propose a low-rank matrix factorization and completion framework which jointly tackles both the demosaicing and the unmixing steps of the SSI data. In addition to a "natural" technique, we expand the well-known pure pixel assumption to the SSI sensor level and propose two dedicated methods to extract the endmembers. The first one can be seen as a weighted Sparse Component Analysis (SCA) method, while the second one relaxes the abundance sparsity assumption of the former. The abundances are then recovered by applying the naive approach with the fixed extracted endmembers. Finally, we experimentally validate the merits of the proposed methods using synthetically generated data and real images obtained with an SSI camera.**

***Index Terms*—Snapshot Spectral Imaging, Unmixing, Demosaicing, Low-Rank Approximation, Sparsity.**

I. INTRODUCTION

STATE-OF-THE-ART Hyperspectral Imaging (HSI) architectures can be categorized into spatial, spectral, and frame scanning approaches [1]. Regardless of the chosen approach, the primary potential of all these methods lies in the capability to obtain images with enhanced spectral, spatial, and temporal resolutions. Nonetheless, a common characteristic across all scenarios is the necessity for repeated scanning of the scene and the acquisition of numerous exposures (frames) to compile the full spatio-spectral resolution data cube coupled with considerations regarding the cost and size of the camera. A new generation of HSI imaging architectures, known as Snapshot Spectral Imaging (SSI), has been introduced to address the challenges mentioned earlier [2]. SSI enables the efficient acquisition of the spatio-spectral content of dynamic scenes using miniaturized platforms, and it can acquire the complete cube from a single or a few exposures. To accomplish this objective, SSI architectures associate each spatial pixel with a specific spectral band, hence introducing a crucial trade-off between spatial and spectral resolution [3]. These cameras can capture videos with a high frame rate, and they are helpful in the case where the motion is unpredictable, and the camera/object is moving in 2D or 3D, such as in robotic applications or lane sorting [4].

Among the recent strategies that have emerged, SSI cameras utilizing Fabry-Perot filters (FPf) [5] and compressive coded-aperture SSI (CASSI) systems [6] only produce a 2-D image derived from the 3-D hyperspectral data. For both types of cameras, a post-processing technique called "demosaicing" is required to estimate the complete hyperspectral data cube. However, the two sensing technologies differ in their design and associated demosaicing approaches. In this paper, we focus on the cameras using FPf. Various approaches have been proposed to perform demosaicing. These approaches can be classified into two categories, including "traditional" methods [3], [7]–[11] and deep-learning-based strategies [12]–[17].

On the other hand, hyperspectral unmixing is one of the primary methods for analyzing hyperspectral images. It breaks down a mixed pixel into a set of component materials, each weighted by their respective proportions. To accomplish this, multiple algorithms for hyperspectral unmixing have been developed, typically encompassing two stages: endmember extraction and mixed-pixel decomposition. The methods for identifying endmembers include, e.g., N-FINDR, Pixel Purity Index (PPI), or Vertex Component Analysis (VCA) [18]. Additionally, Nonnegative Matrix Factorization (NMF) [19] is a commonly applied approach in unmixing scenarios. NMF aims to learn a part-based representation of the data, aligning with the cognitive process of how the brain identifies objects. Finally, Sparse Component Analysis (SCA) [20] is another widely used family of unmixing methods and has been applied to HSI unmixing, e.g., in [21], [22].

However, as Tsagkatakis et al. [3] have stated that applying classification directly on SSI images post-demosaicing often leads to unsatisfactory performance. Contrastingly, most existing unmixing methods are designed to work on fully reconstructed data cubes and do not account for the inherent missing entries typical in snapshot imaging scenarios. Furthermore, in the context of *in-situ* mobile sensor calibration, it has been demonstrated that a combined approach of low-rank matrix completion and factorization is significantly more efficient than a sequential two-stage process of matrix completion followed by factorization [23].

K. Abbas, M. Puigt, G. Delmaire, and G. Roussel are with Univ. Littoral Côte d'Opale (ULCO), LISIC – UR 4491, F-62219 Longuenesse, France, e-mail: firstname.lastname@univ-littoral.fr.

This work was partly funded by the Région Hauts-de-France. Experiments presented in this paper were carried out using the CALCULCO computing platform, supported by ULCO.

This gap in methodology underscores a crucial limitation in current practices, where the intricate balance between demosaicing and unmixing is not adequately addressed.

Recognizing this issue, our proposed approach seeks to perform demosaicing and unmixing jointly. This integrated methodology aims not only to enhance unmixing results but also to maintain optimal demosaicing performance.

In the first part of this paper, our contributions to the field of Snapshot Spectral Imaging (SSI) are outlined as follows:

- We concentrate on establishing a general framework for demosaicing images, applicable to various Multispectral Filter Arrays (MSFAs) [24]. This broad-scope framework sets the foundation for our comprehensive methods in "demosaicing" and "unmixing" hyperspectral images captured by SSI cameras.
- Our investigation is driven by the hypothesis that combining low-rank matrix completion and factorization is more efficient than a two-stage process involving these components separately.
- Three innovative methods are proposed for RAW SSI image demosaicing and unmixing:
  - The first is a Naive approach directly derived from Weighted NMF (WNMF).
  - While building on the Naive approach, the second and third methods operate under the assumption of sparsity within sensor 'patches' mainly dominated by a single unique endmember. These methods differ in their assumptions and treatment in cases involving multiple endmembers.
  - The second and the third methods incorporate (i) rank-1 WNMF within the "patches", (ii) a single-source confidence metric, (iii) an endmember extraction phase, and (iv) a final abundance estimation step.
- Performance evaluations are conducted on both SSI simulations—derived from synthetic images and the Columbia CAVE Dataset [25]—and real SSI images from the Hyko 2 dataset [26].

Building on the general framework established in this part of the paper, Part II of our work [27] explores the complete pipeline provided by the camera manufacturer, focusing on new unmixing approaches for RAW SSI images. This part is designed specifically for applications involving Fabry-Perot filters or MSFA sensors with less selective filters, addressing complex scenarios often encountered in practice.

Please note that the naïve WNMF method and a preliminary version of the second proposed method mentioned above were proposed in [28]. This first part of the paper differs from [28] as follows. We significantly refine the method by mainly improving the abundance estimation and clustering stages. We incorporate new techniques and insights from further research and experimentation, enhancing the method accuracy, robustness, and applicability.

The remainder of the paper is organized as follows. Section II presents the snapshot mosaic sensor with the existing work for demosaicing SSI data and for unmixing multi- and hyperspectral images. Next, in Section III, we present the problem of joint unmixing and demosaicing. Section IV introduces our proposed methods, the performances of which are assessed in Section V. Finally, we conclude our discussion and introduce future directions for research in Section VI. A table of notations used throughout this paper is provided in Table I for clarity and ease of understanding.

TABLE I
TABLE OF MATHEMATICAL NOTATIONS

Notation	**Description**
Y	Matrix
$\hat{Y}$	Estimated Y matrix
$\bar{Y}$	Matrix Y after changing its size.
$\underline{g}$	Column vector
$\circ$	Hadamard product
f	Row vector
$\|\cdot\|_F^2$	The Frobenius norm
$\mathbb{1}_{(m\cdot n)\times k}$	$(m\cdot n)\times k$ matrix of ones
$\approx$	Approximately equal
$\gg$	Much greater than
$\mathbb{F},\mathbb{X}$	Pool of the spectra

II. RELATED WORK

A. Hyperspectral Imaging and Snapshot Spectral Imaging

Hyperspectral Imaging (HSI) is an analytical technique based on spectroscopy, which involves capturing hundreds of images at various wavelengths for the same spatial region. Hyperspectral imaging records the complete light spectrum for every pixel within a scene, providing high-quality wavelength resolution, encompassing both the visible and near-infrared spectra. The gathered data forms a hyperspectral cube, where two dimensions define the spatial dimensions of the scene, and the third dimension represents its spectral content. [18], [29].

A fundamental challenge that HSI sensors must address is how to acquire three-dimensional HSI data, encompassing two spatial dimensions and one spectral dimension, using a single detector, such as a 1D-array or 2D-plane detector. Thus, different strategies in HSI acquisition designs have emerged, leading to wavelength-scanning, point-scanning, and line-scanning acquisition methods [29], [30]

Current spectral camera systems are slow, usually taking seconds to minutes to scan an object. Furthermore, most are not portable to be placed on drones or unmanned aerial vehicles (UAVs). Portability involves not only the size of the devices but also their platform configuration as either being bench-top systems for use in a laboratory environment or deployed instruments for in-field analysis [31]. Therefore, technological advances have enabled fast, miniaturized, and low-cost spectral cameras, i.e., snapshot spectral cameras using Fabry-Perot filters (FPf) and compressive coded-aperture SSI (CASSI) systems. Both designs acquire only a 2-D image, and post-processing is required to restore the full data cube.

SSI cameras that utilize Fabry-Perot filters (FPf) are designed by monolithically integrating optical interference filters onto conventional CMOS image sensors [32]. The Fabry-Perot filter (FPf) is a widely employed tool for directing and measuring the wavelengths of light in systems that require compact, integrated, and highly tunable spectral filtering capabilities. The FPf filter is made of a transparent layer (or cavity) with two mirrors on each side of that layer. The cavity

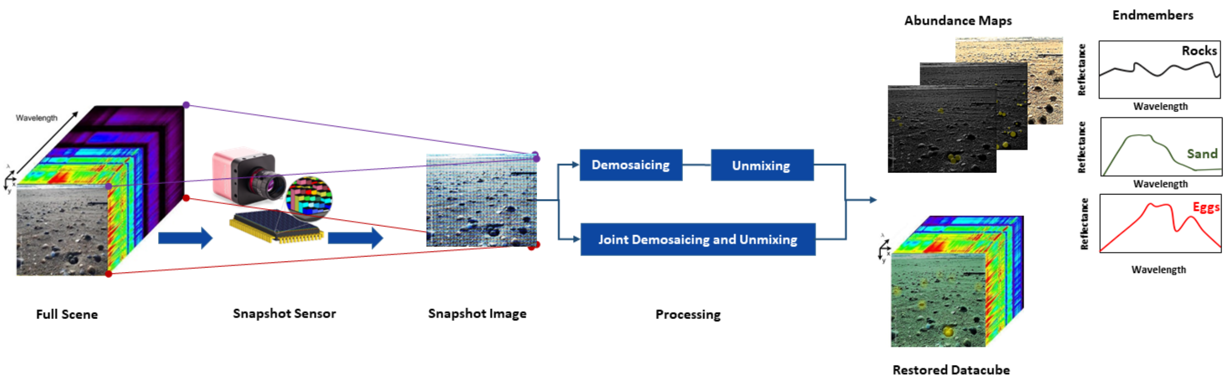

Fig. 1. Overview of acquisition and processing on a scene contains three endmemebers (sand, rocks, and eggs). The SSI image can be processed either by a two-stage approach or by applying unmixing and demosaicing jointly to restore the data cube, extract the endmembers, and find the abundance maps.

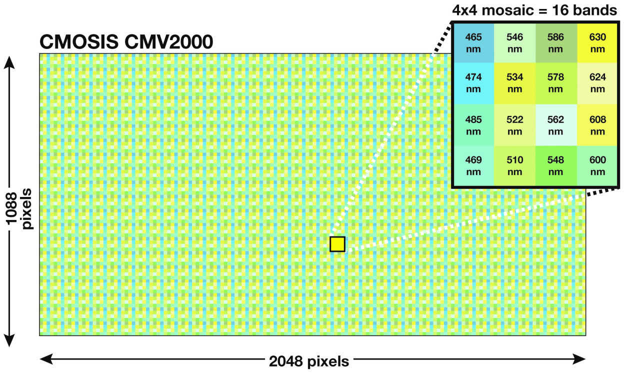

Fig. 2. Snapshot mosaic filter layout (Source IMEC)

length and the mirror reflectivity determine the filter's selected wavelength and the spectral bandwidth (or full width at half maximum), respectively [5], [32], [33].

The filter layout describes the pattern in which the filters are deposited on the sensor, and currently, there are two snapshot FPf designs, i.e., snapshot tiled and snapshot mosaic. The snapshot tiled filter layout has an area design where the filters are organized in rows and columns of tiles, all with a fixed width and height. Each band image of a filter corresponds to one tile on the active area. In order to get a full data cube, the optical system needs to replicate the image to each tile [34]. The snapshot mosaic filter layout has a per-pixel design. The basic FPf structure is extended into a set of filters by varying the cavity length for each pixel-level within a $\sqrt{k} \times \sqrt{k}$ filter cell ($\sqrt{k}$ could be 3, 4, or 5) [5], [32]. This mosaic pattern, also known as a sensor patch, is replicated across the entire active area of the sensor surface. The organization of the filters in the mosaic pattern is shown in Fig. 2. Due to its design and contrary to the tiled filter, it can be used with a standard optical system.

Coded aperture snapshot spectral imagers (CASSI) is a snapshot imaging technology that employs compressive sensing to capture the full data cube in just a few measurements and, in some cases, a single shot [6]. It aims to overcome the limitations of the spatial versus spectral resolution multiplexing trade-off by spatially undersampling the scene in each band and using compressive sensing to reconstruct the full spatial resolution. The concept of compressive sensing replaces the spatial versus spectral resolution trade-off with a signal-dependent spatial resolution versus image quality trade-off, which often results in unpredictable quality and introduces spatial and spectral reconstruction artifacts [35].

The three aforementioned snapshot imaging technologies, including CASSI systems, aim to generate a data cube from a single shot without scanning, each with its unique technology, design, and processing methods. While we acknowledge the numerous potential advantages of CASSI systems, our focus in this work is specifically on processing snapshot mosaic cameras based on Fabry-Perot filter technology. To the best of our knowledge, no commercially available CASSI cameras are on the market. In contrast, snapshot multispectral cameras using IMEC Fabry-Perot filters are commercially available, with three manufacturers currently offering such cameras. This availability directly influences our research scope, allowing us to conduct hands-on experiments and analysis with the technology at our disposal. While some work has been done using Compressed Sensing (CS), e.g., in the studies by Wang et al. [36] and Vargas et al. [37], these approaches are only applicable to specific in-laboratory hardware and remain distinct from our practical focus on snapshot mosaic cameras utilizing Fabry-Perot filter technology. Therefore, while acknowledging the broader landscape of snapshot imaging technologies, our study focuses on the practical and accessible realm of Fabry-Perot filter-based snapshot mosaic cameras.

B. Demosaicing Methods

Demosaicing is a well-studied problem in the field of imaging, particularly for RGB color images, where the challenge arises from the presence of Bayer-structured filters that sample the three primary colors. In the case of SSI images, the camera associates each spatial pixel with a specific wavelength. The straightforward method for generating the entire hyperspectral cube from a single snapshot image involves grouping the suitable number of pixels with a corresponding reduction in spatial resolution. For the 16-band case for example, groups of 4×4 pixels are collapsed into a single "super-pixel", incurring a 93.75% reduction in spatial resolution [3]. However, the demosaicing stage aims to generate the entire HS data cube and conserve the spatial resolution. Therefore, various approaches for estimating the missing information have been proposed. These approaches can be classified into two categories, i.e., "traditional" methods and deep learning-based strategies.

"Traditional" demosaicing methods refer to non-deep-learning-based approaches that use spatial and/or spectral correlation. In [7], a weighted bilinear interpolation method was proposed. It employes a two-step process in which, for each spectral band, a sparse raw image containing only the observed measurements is reconstructed. Then, the demosaicing is achieved through convolution with a low-pass filter that is normalized to address the missing measurements. Mizutani *et al.* [9] proposed an extension—termed Iterative Spectral Difference (ItSD)—with better performance especially when there is a cross-correlation between the images under different wavelengths. Miao *et al.* [8] proposed a method divided into four steps for 4×4 filter pattern where at each step t, 2^t values become known, either because they are already the acquired values by the camera or previously estimated. A multispectral demosaicing approach using a pseudo-panchromatic image (PPID) was proposed by Mihoubi *et al.* [10] where the panchromatic image is spatially defined from the raw image and is used to estimate each channel.

The authors in [11] proposed a generalized demosaicing method with structural and adaptive nonlocal optimization for regular filters and new theoretical proposed filters. Tsagkatakis *et al.* [3] proposed a novel method to solve the problem of demosaicing using low-rank matrix completion with more realistic spectral sensitive functions (SSFs) to model the spectral correlation and the harmonics produced by the camera filter. Recently, Rathi *et al.* [38] introduced two novel demosaicing methods for multispectral images, PCWB and PCBSD, emphasizing spatial correlations and enhancing spectral difference, respectively. Another approach by Rathi *et al.* [39], GMD-SCPPI, employs a pseudo-panchromatic image for enhanced multispectral image reconstruction. Subsequently, Gupta *et al.* [40] contributed an adaptive and progressive demosaicing approach distinguished by its application of a progressive adaptive interpolation strategy. Additionally, Zhang *et al.* [41] proposed GMDICC, which improves spatial and spectral reconstruction quality in MSFA imaging systems by combining gray correction, wavelet transform, and iterative channel reconstruction.

Deep learning methods incorporate large-scale network training to improve the process of demosaicing. In [12] a framework using convolutional neural networks was developed involving the process of demosaicing and removing the crosstalk in the image. A deep convolutional network for snapshot hyperspectral demosaicing was proposed in [13], while joint demosaicing and denoising for CFA and MSFA images using a mosaic-adaptive dense residual network was proposed in [14]. Recently Feng *et al.* [15] proposed a mosaic convolution network for demosaicing multispectral filter array images, where attention framework has been used to improve the process of demosaicing. While deep learning methods have demonstrated superior performance in demosaicing tasks, they can have limited generalization and require large amounts of training data compared to the above blind methods, which work non-supervised [11]. Therefore, in this work, we focus only on studying the performance of the traditional approaches.

C. Unmixing Methods

Hyperspectral unmixing (HU) involves the separation of pixel spectra from a hyperspectral image into a group of endmembers and a series of fractional abundances. The endmembers represent the pure materials in the image, and the abundances at each pixel represent the percentage proportion of the presence of each endmember in the pixel [18]. Mainly, unmixing algorithms can be divided into four categories[1]: geometrical, sparse regression-based, deep learning (DL)-based, and statistical methods [42].

Geometrical approaches, divided into Pure Pixel (PP) and Minimum Volume (MV) methods, rely on simplex models or positive cones. PP methods, including the pixel purity index and vertex component analysis (VCA), assume at least one pure pixel per endmember [18]. MV methods minimize simplex volume [43]–[45]. Sparse Component Analysis (SCA) for Blind Source Separation (BSS) detects single-source zones, categorized into 1-sparse and q-sparse methods, based on the assumption of single or multiple active endmembers in image areas [20], [46], [47].

Sparse regression-based methods, using spectral libraries, assume linear combinations of pure spectral signatures [48]–[51]. Deep learning methods, particularly autoencoders, have shown promise in HU but require extensive training [42], [52]–[54].

Statistical methods, like Independent Component Analysis (ICA) and Nonnegative Matrix Factorization (NMF), address highly mixed data when geometrical methods are insufficient. Modified ICA and various forms of NMF, including constrained, structured, and generalized NMF, adapt to specific HU challenges [42], [55]–[66].

From another perspective, modeling the mixture of spectra in each pixel may result in two different linear and nonlinear models, respectively. Both models address different degrees of light-material interaction. Bilinear and linear-quadratic models tackle nonlinearity effectively [67]–[69].

Finally, the endmembers can be significantly affected by atmospheric, illumination, or environmental variations within an image. Unfortunately, traditional spectral unmixing algorithms disregard the spectral variability of the endmembers, which reproduces significant errors throughout the whole unmixing process and compromises the quality of its results. Therefore, multiple methods have been proposed to take spectral variability into account [70]. Ge Zhang et al. [71] proposed a convex optimization-based method for spectral variability-augmented reconstruction. Hongyi Liu et al. [72] introduced a wavelet domain approach with Bayesian methods for more accurate spectral variability handling.

III. PROBLEM STATEMENT

As previously mentioned, the considered SSI technology operates on a mosaic of Fabry-Perot filters, allowing each camera

---

[1] Another taxonomy is also possible, depending if the considered methods are blind (i.e., geometrical and statistical methods) or supervised.

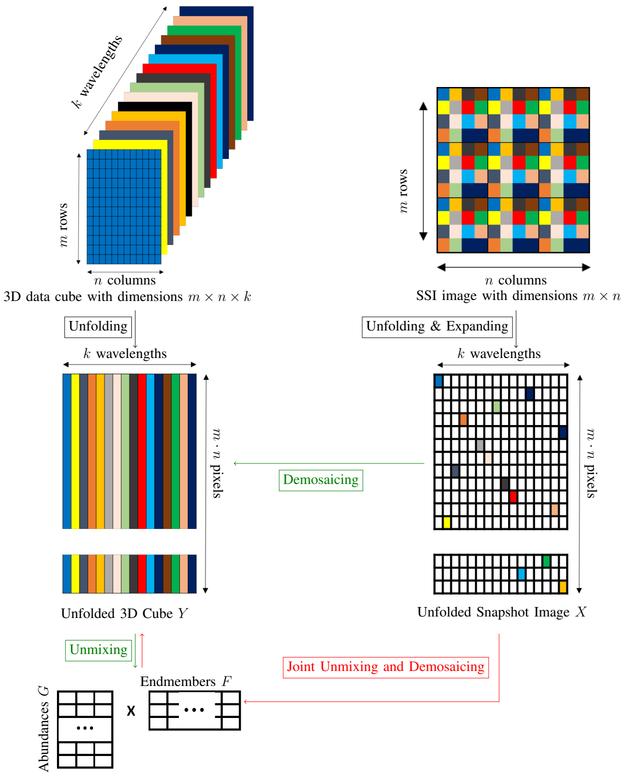

Fig. 3. Principles of the two-step (in green) and joint (in red) strategies.

pixel only to capture one unique narrow band of wavelengths in the ideal case. Unmixing the SSI images requires processing the images to build the 3-D data cube. However, Tsagkatakis *et al.* [3], performed classification on the demosaiced images and reported a low performance with a significant gap between the average estimation accuracy and the intended one. On the other hand, in the context of *in situ* mobile sensor calibration, it was found that incorporating low-rank matrix completion and factorization demonstrated significantly more efficient than employing a two-stage approach involving low-rank matrix completion followed by matrix factorization [23]. Accordingly, we aim to apply the unmixing and demosaicing jointly, starting from the raw SSI data (see Fig. 3). So in this section, we define the SSI system and the joint demosaicing and unmixing problem we aim to solve.

Formally, an SSI camera captures a two-dimensional image consisting of $m \times n$ pixels for each exposure, where m and n represent the pixel counts in the horizontal and vertical dimensions, respectively. Each of the spatial pixels among the $m \cdot n$ available ones corresponds to a distinct spectral band from a total of k bands expected to be acquired by the camera. More specifically, this signifies that an SSI image can be seen as a two-dimensional projection of a theoretical 3D data cube with dimensions $m \times n \times k$, which we will now formalize and model.

Following an unfolding strategy commonly utilized in unmixing, we express the theoretical 3D data cube as an $(m \cdot n) \times k$ matrix whose rows correspond to spatial positions while column indices are linked to wavelengths. As suggested in [3], it becomes feasible to create a data matrix of dimensions $(m \cdot n) \times k$ denoted as X, which contains missing entries. Both matrices X and Y are linked through

$$W \circ X = W \circ Y, \tag{1}$$

where W represents a binary weight matrix, with its non-zero entries indicating the wavelengths observed by the camera, Y is the unfolded 3D data cube, X is the unfolded and expanded SSI image—so that X and Y share the same dimensions, see Fig. 3—and the symbol $\circ$ signifies the Hadamard product between matrices. Similarly, applying the unfolding process to the $m \times n$ SSI image, as we did for the data cube Y, results in an $(m \cdot n) \times 1$ vector denoted as $\underline{z}$. In this vector, the i-th entry corresponds to the non-null value found in the i-th row of X. Since the binary weight matrix W is known, obtaining X from $\underline{z}$ is a straightforward process and vice-versa. Hence, we can assume that X represents the original data matrix derived from the SSI acquisition process. The process of retrieving Y from X corresponds to "demosaicing" the SSI image. In practice, this can be addressed by, e.g., incorporating the assumption that Y is low-rank [3].

Additionally, we make the assumption that every row of Y can be represented as a linear mixture of the spectra corresponding to the materials observed by the camera—a.k.a. endmembers—i.e.,

$$Y \approx G \cdot F, \tag{2}$$

where F represents the $p \times k$ matrix of endmembers, G represents the $(m \cdot n) \times p$ abundance matrix, and p represents the number of endmembers present in the scene. Equation (2) is not only a very classical model met in hyperspectral unmixing [18] but also a low-rank approximation model, provided $p < \min\{(m \cdot n), k\}$. Combining Eqs. (1) and (2) provides the considered joint "demosaicing" and "unmixing" model, i.e.,

$$W \circ X \approx W \circ (G \cdot F). \tag{3}$$

Indeed, if it was possible to fully estimate both G and F from the partially observed matrix X, then their product $G \cdot F$ is an estimation of Y and one may derive a more accurate one as

$$\hat{Y} = W \circ X + (\mathbb{1}_{(m \cdot n) \times k} - W) \circ (G \cdot F), \tag{4}$$

where $\mathbb{1}_{(m \cdot n) \times k}$ represents the $(m \cdot n) \times k$ matrix of ones. Moreover, the information contained within G and F can be valuable for various applications, such as spectral library learning through the use of F, or for land use/cover analysis derived from G. Once more, it is important to emphasize our objective of comparing the performance between a two-stage strategy—including a demosaicing step where Y is estimated, followed by an unmixing step where G and F are derived (referred to as the green framework in Fig.3)—and a joint demosaicing and unmixing strategy (depicted in red in Fig.3). In Section IV, we introduce three different approaches for this joint strategy.

IV. Proposed Methods

We now present our proposed approaches. In fact, we are proposing three joint demosaicing and unmixing methods. To start with, we introduce a "naïve" approach, derived from weighted NMF, following the strategy presented in [23] for a different application. Subsequently, we propose two novel methods, expressly developed for SSI data.

A. Naive Method

Initially, we introduce a naive method aimed at solving Eq. (3), which is a specific case of Weighted NMF (WNMF). Due to its similarity with low-rank matrix completion [73], the naive approach below can be seen as an alternative to [3] in which the structure of the low-rank matrix to recover is more interpretable. WNMF can be addressed using various strategies, including (i) incorporating the weights into the update rules as proposed in [74], (ii) applying an Expectation-Maximization (EM) Framework as discussed in [73], or (iii) employing stochastic gradient descent while focusing on the available data points. The second strategy, as identified in [73], was reported to be significantly faster and more accurate than the first one. Therefore, we choose this approach.

In the EM strategy, there are two steps—i.e., the E-step and the M-step—which are alternatingly and iteratively run. The E-step aims to estimate the expected complete matrix $\hat{Y}$ with respect to the known data $W \circ X$, the uncertain or unknown matrix data $(\mathbb{1}_{(m\cdot n)\times k} - W) \circ Y$, and the estimates of G and F at the $(t-1)$ iteration, denoted $\hat{G}^{(t-1)}$ and $\hat{F}^{(t-1)}$, respectively. Its solution reads [75]

$$\hat{Y} = W \circ X + (\mathbb{1}_{(m\cdot n)\times k} - W) \circ (\hat{G}^{t-1} \cdot \hat{F}^{t-1}). \tag{5}$$

The M-step then consists of applying standard NMF update rules to $\hat{Y}$ to derive $\hat{G}^t$ and $\hat{F}^t$. Once NMF converged to a given solution [75] or after a given number $\text{Max}_{\text{outIter}}$ of iterations [73], $\hat{Y}$ is updated in another E-step using the last estimates of G^t and F^t [73], [75]. In this work, we choose the Nesterov NMF (NeNMF) method [76] which is run until one of the following stopping criteria is reached: a maximum number of NMF iterations has been run—i.e., 1000 NMF iterations in our experiments—or the approximation error between the complete matrix derived in the E-step and its NMF approximation is below a threshold (i.e., 10^{-5} in our experiments). Meanwhile, when the abundance matrix $\hat{G}^t$ is updated, the sum to one constraint is satisfied by updating $\hat{Y}$ and $\hat{F}^t$ using the same strategy as in [42]. To apply this constraint, we modify the matrices $\hat{Y}$ and $\hat{F}$ by adding an additional column of ones. This modification allows us to control the Abundance Sum-to-One Constraint (ASC) using the parameter δ, which adjusts the influence of the sum-to-one constraint in the optimization process[2]. The augmented matrices $\bar{Y}$ and $\bar{F}$ are represented as follows:

$$\bar{Y} \triangleq \left[\hat{Y} \quad \delta \mathbb{1}^T_{(m\cdot n)\times 1}\right], \quad \bar{F} \triangleq \left[\hat{F} \quad \delta \mathbb{1}^T_{p\times 1}\right] \tag{6}$$

The whole method is provided in Algorithm 1.

B. Locally Rank-1 and Clustering-based Proposed Technique

We now introduce our first proposed method, which originates from the fundamental approach to restoring the data cube. Specifically, the image sensor is divided into patches that are replicated across the sensor surface. Each patch has dimensions $\sqrt{k} \times \sqrt{k}$, with common values for k being 16 or 25 [3]. Therefore, a patch typically measures either 4×4 or 5×5. In this context, it is reasonable to assume that each patch corresponds to a "super-pixel," meaning that each patch is associated with a unique endmember. In practice, such an assumption is not correct, which is why various demosaicing methods have been developed. Nevertheless, this assumption could still be valid for certain patches to find where one endmember significantly dominates over the others. This concept aligns with the pure-pixel assumption [18], or the concept of abundance sparsity in SCA, as described in [20]. However, the primary difference between our problem and the classical unmixing problem lies in the fact that we only have partial observations of the data cube within a patch, and our goal is to estimate it based on a limited number of available samples. This permits us to declare our first assumption.

Assumption 1 (Pure patch assumption)**.** *For each endmember, there exists at least one sensor patch where only this endmember is present.*

Our proposed method is outlined as follows. We denote by X_i, $\hat{Y}_i$, and W_i the $k \times k$ sub-matrices of X, $\hat{Y}$, and W, respectively, corresponding to Patch i. We obtain a rank-1 approximation of $\hat{Y}_i$ from X_i using the aforementioned WNMF strategy[4], which can be expressed as follows:

$$W_i \circ X_i \approx W_i \circ (\underline{g}_i \cdot f_i), \tag{7}$$

where $\underline{g}_i$ represents a $k \times 1$ column vector and f_i represents a $1 \times k$ row vector.

When a patch contains only one dominant endmember, thereby satisfying Assumption 1, the patch itself becomes rank-1. Consequently, the rank-1 approximation derived from partial data in X_i enables us to estimate the endmember f_i. However, when a patch contains multiple endmembers, we must not detect the patch as pure. This leads us to our second assumption.

Assumption 2. *In the patches where several endmembers are present, their abundances significantly vary over each patch.*

Assumption 2 is classically stated in SCA [20]. In practical situations, it is expected that the SSI camera is positioned close enough to the observed scene, so that one may not expect multiple abundances to remain in constant proportions over a patch. Consequently, if the i-th patch under consideration is approximately pure, then

$$\|W_i \circ X_i - W_i \circ (\underline{g}_i \cdot f_i)\|_F^2 \approx 0. \tag{8}$$

Conversely, if this patch is not pure, then

$$\|W_i \circ X_i - W_i \circ (\underline{g}_i \cdot f_i)\|_F^2 \gg 0. \tag{9}$$

---

[2] In our implementation, the value of δ is set to be 15, as this value has been found to provide an effective balance in the optimization process.

[3] As the patch size directly equals the number of wavelength bands, k is consistently used to denote the two elements.

[4] We employ Weighted Nonnegative Matrix Factorization (WNMF) with a Nesterov solver, using Expectation Maximization on each patch, to calculate the rank-1 approximation.

In this context, this type of error can be regarded as a “single-source confidence measure,” corresponding to those commonly employed in SCA. Hence, from each patch, we obtain a noisy estimate of a “true” endmember. The retrieved spectra that satisfy Eq. (8) are gathered and organized into a matrix denoted as $\mathbb{F}$. These estimates are further assumed to be organized as clusters of spectra distributed around the “true” source spectra. Therefore, we can employ any clustering technique, such as K-means or K-medians, initialized with K-means++ [77], to extract the actual endmembers. A refined approach involves identifying the patches where the squared Frobenius norm mentioned above is small-enough[5]. This results in a smaller set of spectra, each of which is closer to the “true” ones. This approach is similar to the *Selective* K-means or K-medians methods proposed in [78] and was found to notably enhance the performance of our proposed method preliminary test[6].

Once the true endmembers are extracted and stored in the matrix F, the abundance matrix G is re-estimated using the Naive method described in Subsect. IV-A, with fixed F and the sum-to-one constraint on the abundance matrix G in the M-step. The whole strategy is provided in Algorithm 3. It is worth noting that the abundance estimation can also be accomplished using the least-squares method, similar to what we applied in the [28]. However, our experiments discovered that running the Naive WNMF yields more accurate results

C. Method with Relaxed Abundance Sparsity Assumption

We now introduce our third approach. It may be seen as an extension of the previous one as it also assumes Assumption 1 to be valid. However, it significantly relaxes Assumption 2 which is replaced by the following one.

Assumption 3. *In the patches where several endmembers are present, their abundances may or may not vary over each patch.*

This assumption states that in the patches where multiple endmembers are present, we do not require any constraint on their abundances. Consequently, Eq. (8) is satisfied if the patch is pure (Assumption 1) or, when several endmembers are present in a patch, their abundances do not vary within the considered patch. Still, Eq. (9) occurs in patches where several endmembers are present and have their abundance proportions to vary over the considered patches. As a consequence, the KPWNMF method cannot be applied with such assumptions and a refined strategy must be proposed.

As for KPWNMF, we collect all the spectra f_i which are estimated in patches where Eq. (8) holds[7] and we arrange them in a matrix denoted $\mathbb{X}$. As explained above, each row vector of this matrix is either an estimate of an endmember of F or a mixture of them. As we assumed an LMM, this matrix can be written as

$$\mathbb{X} = \mathbb{G} \cdot F. \tag{10}$$

Due to Assumption 1, each row of F exists at least once in $\mathbb{X}$ and the estimation of F can be done by applying a pure pixel based method[8], e.g., VCA [79] or SPA [80]. Moreover, $\mathbb{G}$ represents a specific abundance matrix associated with the spectral data in $\mathbb{X}$. It differs from the final abundance matrix G but is derived by selecting rows corresponding to the chosen patch indices in $\mathbb{X}$.

Once the true endmembers are extracted and stored in the matrix F, the abundance matrix G is re-estimated using the Naive method described in Subsect. IV-A, with fixed F and the sum-to-one constraint on the abundance matrix G in the M-step. The whole strategy is provided in Algorithm 4.

In conclusion, we proposed two frameworks, KPWNMF and VPWNMF. They both use spectra estimated in patches where the rank-1 approximation error is low, making their first stages similar. However, they differ in the final stage:

- Thanks to Assumption 2, we know that all the spectra kept in $\mathbb{F}$ correspond to tentative estimates of the actual endmembers in F. Consequently, we can apply any clustering technique to derive F from $\mathbb{F}$, as it is classically done in SCA.
- When Assumption 2 is not met—i.e., when Assumption 3 is stated—some kept spectra might be linear mixtures of the actual endmembers. This is why we here named the pool of kept spectral $\mathbb{X}$. We could propose an outlier robust clustering method to process these data to derive F, provided the number of mixed spectra in $\mathbb{X}$ is low. Instead, as its assumptions are satisfied in $\mathbb{X}$ and as it is not sensitive to the number of mixed spectra, we used VCA instead.

D. Algorithms

This section introduces the pseudo code for our three proposed methods. While these algorithms share several procedural steps, they fundamentally differ in their methodologies, as previously discussed. Algorithm 1 details our Naive WNMF approach, serving as the fundamental framework for the following methodologies. Algorithm 2 introduces the shared patch processing steps essential to both the K-means Patch-based WNMF (KPWNMF) and the VCA Patch-based WNMF (VPWNMF), focusing on the extraction of tentative endmembers. Building upon this, Algorithm 3 and Algorithm 4 diverge to apply specific endmember extraction techniques, and the usage of Assumption 2 or Assumption 3.

---

[5] In practice, we keep all the patches where the rank-one approximation error is below a user-defined threshold. Estimating the optimal threshold value is out of the scope of this paper. In the experiments provided in Sect. V, it is set as the median of all the patch norm errors.

[6] It is noteworthy that K-medians with ℓ_1 norm is used for the clustering stage because it performs slightly better than K-means. It tries to find p median points in the data such that the ℓ_1 distances from each data point to its closest median are minimized. Moreover, the clustering process is repeated several times—e.g., 10 times—and the solution with the lowest within-cluster sums of point-to-centroid distances is selected as the optimal solution.

[7] As for KPWNMF, we only keep spectra estimated in patches where the approximation error is below the median of all the patch norm errors.

[8] We selected VCA because it performed slightly better than the other methods in some preliminary tests.

Algorithm 1 Naive Method

Inputs:
X represents the unfolded SSI image with a rank of p and is weighted by matrix W.
Outputs:
$\hat{Y}$ signifies the reconstructed unfolded data cube.
$[G, F]$ represents the final abundances and endmembers.
Processing:

```
Initialize $G$ and $F$
for $t = 1$ to $\mathrm{Max}_{\mathrm{outerIter}}$ do
    $\hat{Y} = W \circ X + (\mathbb{1} - W) \circ (G \cdot F)^{t-1}$
    for Counter $= 1$ to $\mathrm{Max}_{\mathrm{innerIter}}$ do
        Update $G$ from $\hat{Y}$ and $F$ using NeNMF
        Update $F$ from $\hat{Y}$ and $G$ using NeNMF
```

Algorithm 2 Rank-one patch detection and spectra estimation method used in both proposed KPWNMF and VPWNMF

Inputs:
X represents the unfolded SSI image with a rank of p and is weighted by matrix W.
nb_patches denotes the number of patches to be processed.
Output:
Matrix $\mathbb{M}$ containing the "best" vectors—according to Eqs. (8) and (9)—
for further processing.
Processing:

```
for $i = 1$ to nb_patches do
    Let the submatrices $X_i$ and $W_i$ linked to Patch $i$
    Initialize $\underline{g}_i$ and $f_i$
    for $t = 1$ to $\mathrm{Max}_{\mathrm{outerIter}}$ do
        $X_i^{\mathrm{Comp}} = W_i \circ X_i + (\mathbb{1}_{k \times k} - W_i) \circ (\underline{g}_i \cdot f_i)$
        for Counter $= 1$ to $\mathrm{Max}_{\mathrm{innerIter}}$ do
            Update $\underline{g}_i$ from $X_i^{\mathrm{Comp}}$ and $f_i$ using NeNMF
            Update $f_i$ from $X_i^{\mathrm{Comp}}$ and $\underline{g}_i$ using NeNMF
Keep the 50% best vectors $f_i$—according to Eqs. (8) and (9)—and organize them into matrix $\mathbb{M}$
return $\mathbb{M}$
```

Algorithm 3 K-means (resp. K-medians) Patch-based Weighted Nonnegative Matrix Factorization (KPWNMF)

Inputs:
Matrix $\mathbb{F}$ the output from Algorithm 2.
Rank p.
Outputs:
$\hat{Y}^{\mathrm{final}}$ signifies the reconstructed unfolded data cube.
$[G, F]$ represents the final abundances and endmembers.
Processing:

```
Call Algorithm 2 to get $\mathbb{F}$
$F = \text{K-means}(\mathbb{F}, p)$ (resp. $F = \text{K-medians}(\mathbb{F}, p)$)
Initialize $G$ of size $(m \cdot n) \times p$
Compute $G$ and $\hat{Y}^{\mathrm{final}}$ using Algorithm. 1 with fixed $F$
```

Algorithm 4 VCA Patch-based Weighted Nonnegative Matrix Factorization (VPWNMF)

Inputs:
Matrix $\mathbb{X}$ the output from Algorithm 2.
Rank p.
Outputs: $\hat{Y}^{\mathrm{final}}$ signifies the reconstructed unfolded data cube.
$[G, F]$ represents the final abundances and endmembers.
Processing:

```
Call Algorithm 2 to get $\mathbb{X}$
$F = \mathrm{VCA}(\mathbb{X}, p)$
Initialize $G$ of size $(m \cdot n) \times p$
Compute $G$ and $\hat{Y}^{\mathrm{final}}$ using Algorithm. 1 with fixed $F$
```

V. EXPERIMENTS AND RESULTS

A. Experimental Setup

To evaluate the effectiveness of the proposed methods, we carry out experiments using SSI simulations generated from synthetic images as well as real SSI images captured by SSI cameras. For the synthetic images, we did two experiments. In the first one, we create one image where assumptions one and two are satisfied, and another where assumptions 1 and 3 are satisfied. Each one has 100×100 pixels with three endmembers, i.e., water, metal, and concrete, whose signatures are taken from [81]. We compare the performance reached with the naive method with our proposed approaches KPWNMF and VPWNMF and seven 2-step demosaicing-then-unmixing methods. For the latter, we consider seven SotA demosaicing methods—i.e., GRMR [3], BTES [8], WB [7], PPID [10], ItSD [9], SAND [11], and PCWB [38]—while in the second step, we unmix the restored data cube Y using VCA for estimating the endmembers and Fully Constrained Least Squares (FCLS) for abundance estimation. To measure the effectiveness of the tested methods, we assess their demosaicing improvements by comparing the estimated Y matrices to the ground truth, utilizing the Peak Signal-to-Noise Ratio (PSNR). For unmixing enhancement, we employ the Signal-to-Interference Ratio (SIR), Spectral Angle Mapper (SAM) for endmember estimation, and Mixing Error Ratio (MER) to measure the quality of abundance maps. We additionally incorporated RMSE for abundance estimation accuracy and running time in seconds to assess computational efficiency

For the second experiment, we aim to validate the demosaicing enhancement provided by the proposed approaches on more challenging data. We provide comparative results with the SoTA methods on the CAVE dataset after simulating the 4×4 and 5×5 SSI images using the same strategy as in [3] with all the images in the dataset. Moreover, using real multispectral images allow us to experimentally investigate the validity of the stated assumptions.

Finally, we used real SSIs taken from the Hyko 2 dataset [26]. The images in the dataset are captured using two snapshot mosaic cameras. It is the first dataset to capture hyperspectral data from a moving vehicle, enabling hyperspectral scene analysis for road scene understanding. The data span the visible and near-infrared spectral ranges, from 400 to 1000 nm.

TABLE II

PSNR, SAM, SIR, MER, RMSE, and Time in seconds obtained for the synthetic images with 5x5 and 4x4 (into brackets) ideal filters. In bold, the highest performance value and for RMSE and Time, the lowest value.

Method	**Image 1 (Assumptions 1 & 2)**						**Image 2 (Assumptions 1 & 3)**					
	PSNR	**SAM**	**SIR**	**MER**	**RMSE**	**Time**	**PSNR**	**SAM**	**SIR**	**MER**	**RMSE**	**Time**
GRMR	27.2 (27.5)	0.3 (0.3)	14.3 (65)	2.1 (1.1)	0.4 (0.4)	1.6 (1.57)	29.7 (33.2)	0.4 (0.2)	12.1 (67)	4.9 (4)	0.3 (0.3)	1.5 (0.3)
BTES	24.1 (24.2)	0.4 (0.3)	13.41 (65.8)	-1.2 (-5.4)	0.5 (0.5)	**0.2 (0.3)**	30 (29.1)	0.4 (0.3)	12.3 (65.5)	-4.5 (-2)	0.4 (0.5)	0.4 (0.3)
WB	26.3 (28.9)	0.3 (0.2)	15.6 (70.2)	-0.45 (1.8)	0.4 (0.4)	**0.2 (0.3)**	30.2 (31.2)	0.4 (0.3)	18.2 (63.2)	4.8 (1.5)	0.3 (0.2)	0.3 (0.3)
PPID	30.3 (30.2)	0.06 (0.06)	34.7 (85.9)	9.9 (9.8)	0.3 (0.3)	0.3 (0.3)	34.8 (38)	0.08 (0.05)	31.7 (86)	9.2 (14.9)	0.3 (0.2)	0.3 (0.3)
ItSD	24.5 (23.9)	0.7 (0.6)	8.2 (55.7)	0.5 (-7.4)	0.4 (0.4)	**0.2 (0.3)**	26.4 (26.1)	0.4 (0.5)	8 (56)	-2.4 (-2.08)	0.4 (0.2)	0.3 (0.3)
SAND	30 (30.1)	0.1 (0.1)	31.2 (80.1)	11.3 (9.1)	0.2 (0.2)	3720 (2800)	35.4 (36.9)	0.1 (0.1)	32 (82)	10 (13.2)	0.2 (0.1)	3660 (2500)
PCWB	28.6 (20.3)	0.1 (0.2)	31.7 (70.3)	9.7(9.4)	0.2 (0.3)	0.2 (0.2)	31 (20.2)	0.4 (0.3)	15.5 (71.8)	1.2 (4)	0.4 (0.2)	0.2 (0.2)
Naive	32.5 (32.7)	0.2 (0.2)	19.8 (68.7)	9.2 (8.5)	0.3 (0.3)	15 (12)	34.5 (34.4)	0.2 (0.3)	21.5 (67.2)	10.7 (5.4)	0.3 (0.2)	15 (12)
KPWNMF	**36.5 (35.5)**	0.01 (0.007)	50.2 (103.5)	**16.0 (14.8)**	**0.2(0.2)**	6 (6)	40.3 (40.4)	0.003 (0.006)	50.3 (102.5)	20.9 (19.7)	**0.1 (0.1)**	6 (6)
VPWNMF	35.9 (33.7)	**0.002 (0.003)**	**59.9 (111.0)**	14.7 (12.8)	**0.2(0.2)**	5 (5)	**41.4 (40.8)**	**0.0006 (0.001)**	**75.8 (117.0)**	**21.0 (19.7)**	**0.1 (0.1)**	5 (5)

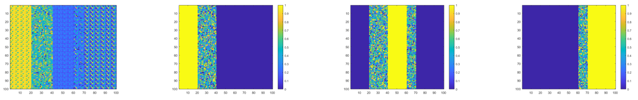
(a) SSI Image (b) Water (c) Metal (d) Concrete

Fig. 4. Image 1, SSI image where assumptions 1 and assumption 2 are satisfied with abundance maps of the three endmembers.

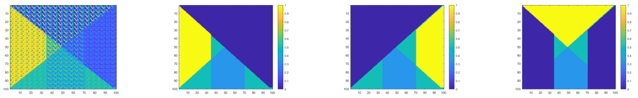
(a) SSI Image (b) Water (c) Metal (d) Concrete

Fig. 5. Image 2, SSI image where assumptions 1 and assumption 3 are satisfied with abundance maps of the three endmembers.

B. Performance evaluation on synthetic images for the ideal case

In the first set of experiments, we generated an image (available on Fig. 4) that fulfills Assumptions 1 and 2, and another image (see Fig. 5) that satisfies Assumptions 1 and 3. Both images have a resolution of 100×100 pixels and are composed of three endmembers—i.e., water, metal, and concrete—with signatures sourced from [81]. In this simulation, we consider the ideal case where each filter associated with each detector element corresponds to an ideal filter with perfect cut-off characteristics, which allow light from a single wavelength to be captured by the detector element. Both images simulate a scene observed from a short distance, implying that many patches are pure. We consider 4×4 and 5×5 spectral filter patterns and investigate the performance of the tested methods under different noise levels.

The PSNR, SAM, SIR, and SAM achieved by all the methods for 4×4 and 5×5 spectral filter patterns are reported in Table II. While the average performance with different noise levels for both images with 4×4 and 5×5 filters is presented in Fig. 6 and Fig. 7, respectively.

A number of key observations can be made from the results presented in the table and the figures:

- The proposed KPWNMF and VPWNMF methods exhibit the highest PSNRs for both images, i.e., the best demosaicing quality. While the demosaicing performance reached with PPID and the Naive method is almost similar, the remaining methods achieve lower reconstruction quality for both images, with WB—i.e., a baseline method—performing similarly to GRMR and ItSD, and with BTES showing the poorest performance. It is important to note that the performance of these methods may vary under different noise levels. Our results show that KPWNMF and VPWNMF continue to significantly outperform the other tested methods until the input SNR is around 25 dB. With lower input SNRS, their performance degrades and both methods provide a similar demosaicing performance as SotA methods.
- In addition to their superior reconstruction quality, the proposed KPWNMF and VPWNMF methods demonstrate the highest performance in endmember identification as measured by the spectral angle mapper (SAM) and signal interference ratio (SIR). Our experimental results show that KPWNMF and VPWNMF achieved the lowest SAM and the highest SIR values among all other methods, indicating their ability to accurately identify endmembers even in the presence of noise. Moreover, our experiments demonstrate that KPWNMF and VPWNMF are robust to noise, maintaining their superior performance even at higher noise levels. Fig. 8 and Fig. 9 show the true and estimated endmembers for both images with the 5×5 filter in the noiseless case. The quality of the restored spectra with the proposed methods is much higher than the 2-stage approach using PPID for demosaicing, the latter being the SotA method to provide the highest unmixing performance.
- The proposed methods KPWNMF and VPWNMF provide the highest MER values among all other methods, indicating their superior abundance estimation performance. Moreover, our experiments demonstrate that KPWNMF and VPWNMF are robust to noise, maintaining their superior performance even at higher noise levels. The comparison between the restored abundance maps and the true abundance maps for both images using the 5×5 filter is shown in Fig.10 and Fig.11 in the noiseless case. As can be seen from the figures, the abundance maps estimated by KPWNMF and VPWNMF are visually closer to the true abundance maps compared to the other methods.
- In addition to MER, our analysis extends to the accuracy of abundance estimation, as measured by RMSE. The RMSE results for the KPWNMF and VPWNMF methods underscore their remarkable precision in estimating

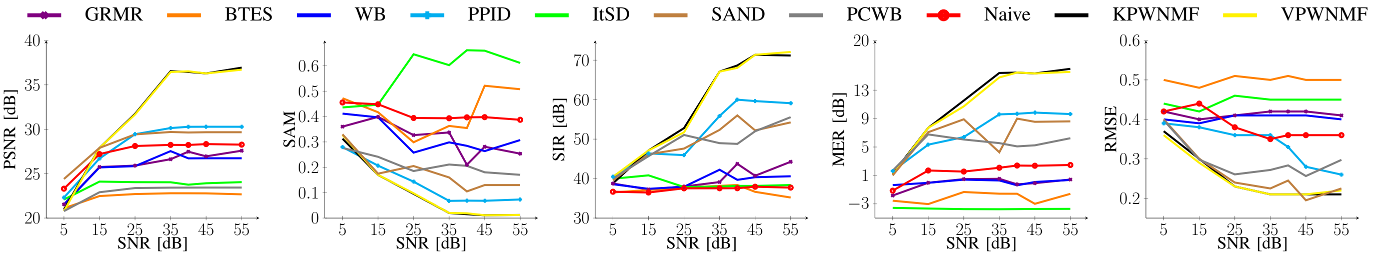

Fig. 6. Mean PSNR, SAM, SIR, MER and RMSE—obtained for Image 1 (Assumption 1&2) with 4 × 4 and 5 × 5 filters—relative to input SNR.

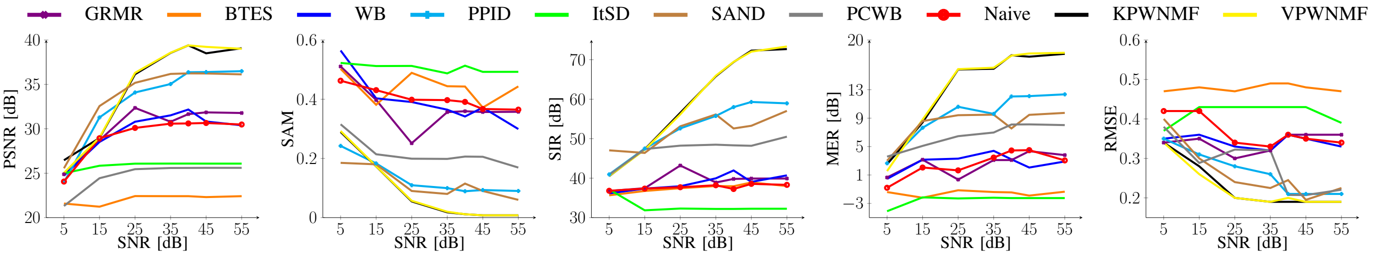

Fig. 7. Mean PSNR, SAM, SIR, MER and RMSE—obtained for Image 2 (Assumption 1&3) with 4 × 4 and 5 × 5 filters—relative to input SNR.

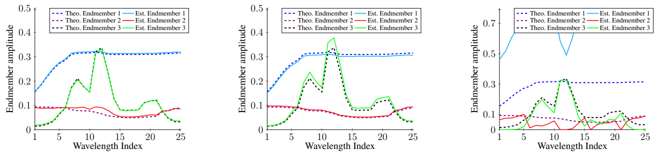

(a) KPWNMF (b) VPWNMF (c) Naive

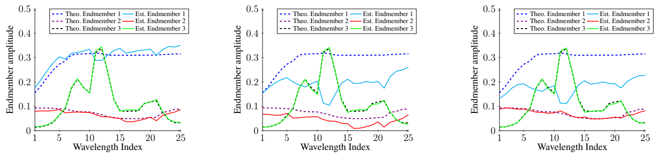

(d) PPID + Unmixing (e) PCWB + Unmixing (f) SAND + Unmixing

Fig. 8. Estimated spectra for the Image 1 with mosaic filter of size 5 × 5.

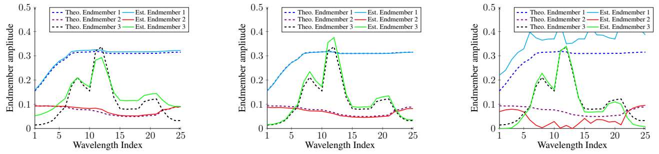

(a) KPWNMF (b) VPWNMF (c) Naive

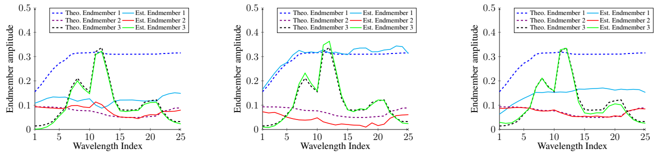

(d) PPID + Unmixing (e) PCWB + Unmixing (f) SAND + Unmixing

Fig. 9. Estimated spectra for the Image 2 with mosaic filter of size 5 × 5.

abundances, shown by the lowest RMSE values among all methods evaluated. While the SAND method exhibits almost similar RMSE performance, a closer examination of the restored abundance maps, as illustrated in Fig.10 and Fig.11, reveals that our methods achieve superior details and quality.

- While evaluating the effectiveness of our proposed KPWNMF and VPWNMF methods, it is essential to consider the computational time alongside other performance metrics. The experimental results indicate that the running time for both methods is notably higher than other evaluated methods. However, it is important to note that the primary focus of this study is to demonstrate the accuracy and effectiveness of these methods in enhancing the quality of demosaicing and unmixing in snapshot spectral imaging. Developing and optimizing the computational efficiency of these algorithms falls outside the immediate scope of this article. Future work will explore strategies to reduce computational time, making these methods more possible for time-sensitive applications.

C. Performance evaluation on CAVE dataset

In addition to the experiments conducted on synthetic images, we evaluated the performance of the proposed methods on the CAVE dataset, which consists of 32 spectral images captured by a multispectral camera in the 400-700 nm range with 10 nm steps. The images have a resolution of 512 × 512 pixels and contain a variety of scenes and objects, making them a suitable dataset for evaluating the performance of multispectral image reconstruction methods. We performed experiments on the CAVE dataset using 4 × 4 and 5 × 5 spectral filter patterns using the same strategy as in [3] with all the images in the dataset and evaluated the PSNR achieved by all the methods for both filter patterns. The results are reported in Table III, where our proposed methods KPWNMF

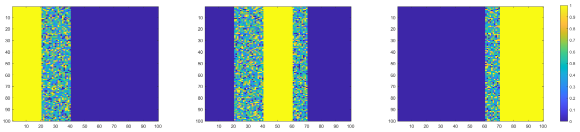

(a) Ground truth

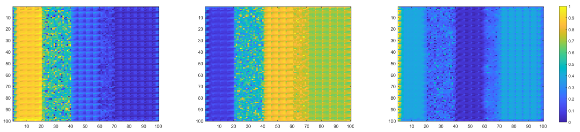

(b) Naive

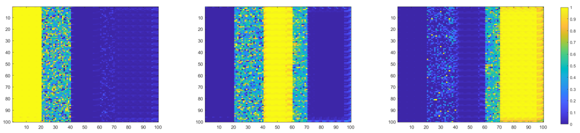

(c) KPWNMF

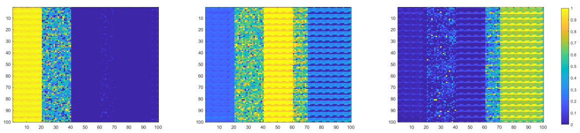

(d) VPWNMF

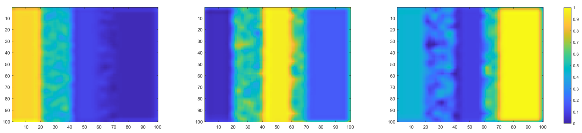

(e) PPID

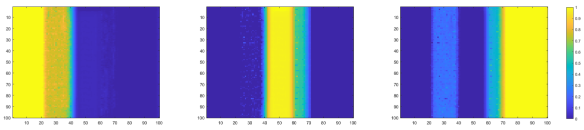

(f) SAND

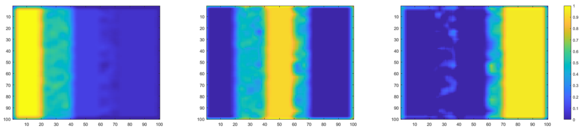

(g) PCWB

Fig. 10. Estimated abundance maps for the Image 1 with 5×5 mosaic filter.

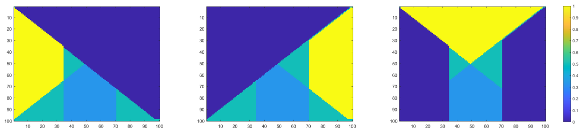

(a) Ground truth

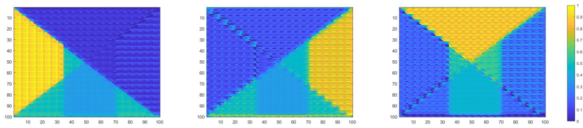

(b) Naive

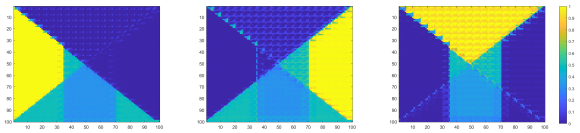

(c) KPWNMF

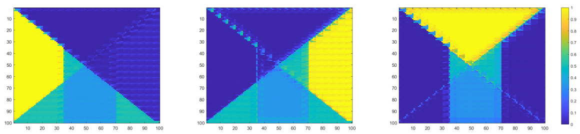

(d) VPWNMF

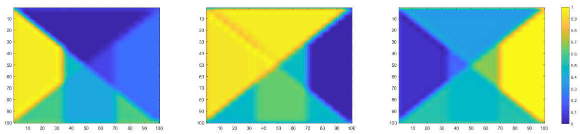

(e) PPID

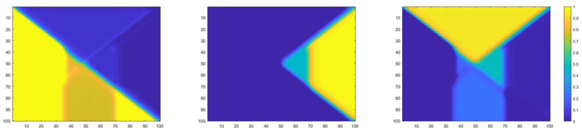

(f) SAND

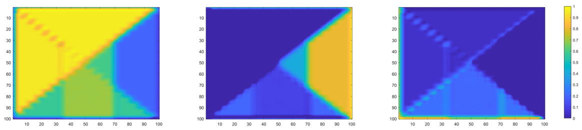

(g) PCWB

Fig. 11. Estimated abundance maps for the Image 2 with 5×5 mosaic filter.

and VPWNMF achieved the highest PSNR values, indicating their superior performance in reconstructing the images. To further evaluate the performance of the proposed methods, we also generated a visual comparison of the restored images using the 4×4 spectral filter pattern. The restored images using KPWNMF, VPWNMF, and other SotA methods are shown in Fig. 12. Our proposed methods demonstrated remarkable results in restoring the details of the images demonstrating their ability to preserve crucial spatial information in the images, which was not effectively captured by the other methods. These results demonstrate the proposed methods' effectiveness in restoring hyperspectral images with complex spectral and spatial information and their superiority over other SotA methods.

D. Performance evaluation on Hyko 2 dataset

We conducted a real data experiment using one image from the Hyko 2 dataset [26], which captures hyperspectral data from a moving vehicle. The dataset[9] contains images captured using two snapshot mosaic cameras and spans the visible

---

[9] The database is accessible at https://wp.uni-koblenz.de/hyko/.

TABLE III
DEMOSAICING PERFORMANCE AVERAGED OVER ALL THE IMAGES IN THE CAVE DATASET. PERF. CRITERION: PSNR (IN DB).

Method	16 bands	25 bands
GRMR	35.3	33.3
BTES	34.7	33.3
WB	35.0	33.4
PPID	37.1	35.4
ItSD	30.2	27.2
SAND	34.2	33.3
PCWB	33.7	33.7
Naive	35.1	34.1
KPWNMF	**37.7**	**35.5**
VPWNMF	**37.7**	**35.5**

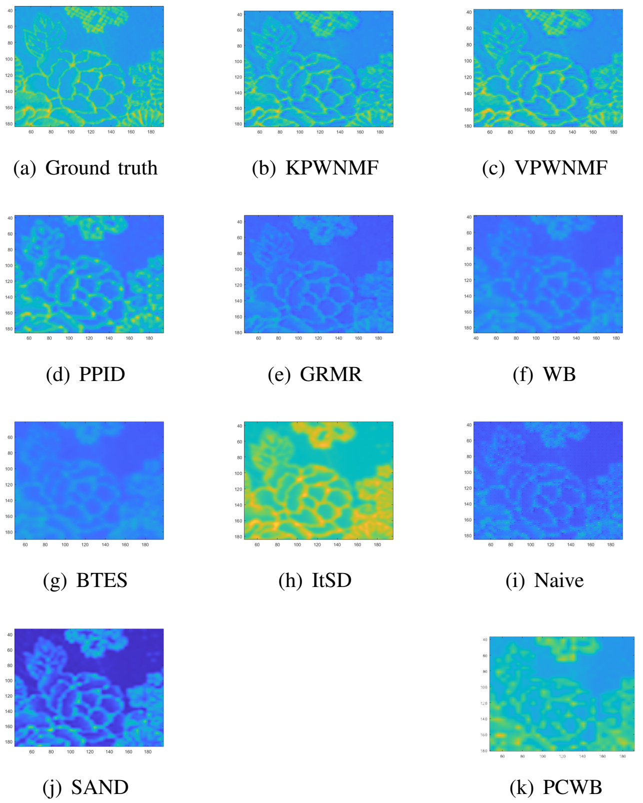

(a) Ground truth (b) KPWNMF (c) VPWNMF

(d) PPID (e) GRMR (f) WB

(g) BTES (h) ItSD (i) Naive

(j) SAND (k) PCWB

Fig. 12. Comparison of the demosaicing performance of all the methods on the Cloths image from the CAVE dataset with 4 × 4 mosaic filter.

and near-infrared spectral ranges from 400 to 1000 nm. We selected one image from the dataset that contained a road, trees, sky, and white signs on the road. As we do not know the real endmembers, we cannot estimate the unmixing accuracy. Instead, we use unmixing to perform image segmentation, as shown in Fig 13. The segmentation is done using the abundance maps generated by each method, where we select the dominant element in each pixel and draw an image showing the segmentation.

Our proposed VPWNMF method—which is based on Assumption 1 and Assumption 3—performed the best among all the methods. It can detect endmembers better than the other methods by using VCA because of the flexibility of Assumption 3. On the other hand, KPWNMF—which is based on Assumption 1 and Assumption 2—only considers the case where the abundance coefficients are significantly changing when there are several endmembers. Therefore, it did not perform as well on this image since the abundance maps were not significantly changing in certain patches. The other SotA methods, including the Naive method, their performance varied and generally fell short in capturing fine details compared to our proposed methods. While VPWNMF was the best-performing method, its performance could have been better, as in some places, the road was classified as the sky. This might be due to multiple issues, e.g., spectral variability, sensor impurities, or nonlinear mixtures in some pixels.

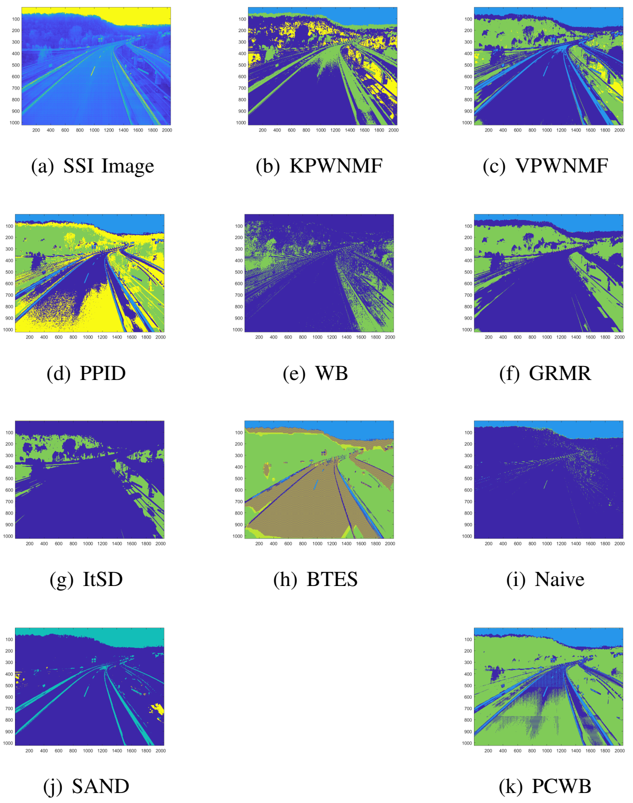

(a) SSI Image (b) KPWNMF (c) VPWNMF

(d) PPID (e) WB (f) GRMR

(g) ItSD (h) BTES (i) Naive

(j) SAND (k) PCWB

Fig. 13. Comparison of the segmentation performance of all the methods on the Hyko 2 Dataset Image.

VI. CONCLUSION AND DISCUSSION

In this work, we aimed to perform "demosaicing" and "unmixing" jointly for the hyperspectral images acquired by the SSI camera. Therefore, we proposed two novel approaches in addition to the naive method derived from Weighted NMF (WNMF). The first one (KPWNMF) assumes that the abundances are sparse in a few patches to find, so that each of these patches is dominated by one endmember. Such an assumption is similarly met with SCA, except that we consider partially observed data. In contrast, the second one (VPWNMF) relaxes the sparsity assumption needed in the latter. We accomplished experiments on SSI simulations derived from synthetic images and real SSI images taken by SSI cameras. Our experimental results showed that the proposed methods outperform the two-stages approaches consisting of applying demosaicing and, after that, unmixing. Moreover, The VPWNMF approach performs better than all the methods on real images due to the flexibility of the assumptions covering more real-life scenarios. However, while our proposed approaches show promising results, there are still challenges to overcome, especially the estimation errors due to spectral variability and the sensor's impurities that we aim to solve in future works.

ACKNOWLEDGEMENT

The authors would like to acknowledge the anonymous reviewers for their valuable comments to improve the present work.

REFERENCES

[1] D. Manolakis, R. Lockwood, and T. Cooley, *Hyperspectral Imaging Remote Sensing*. Cambridge University Press, 2016.

[2] B. Geelen, C. Blanch, P. Gonzalez, N. Tack, and A. Lambrechts, "A tiny VIS-NIR snapshot multispectral camera," in *Advanced Fabrication Technologies for Micro/Nano Optics and Photonics VIII*, vol. 9374, p. 937414, International Society for Optics and Photonics, 2015.

[3] G. Tsagkatakis, M. Bloemen, B. Geelen, M. Jayapala, and P. Tsakalides, "Graph and rank regularized matrix recovery for snapshot spectral image demosaicing," *IEEE Trans. Comput. Imaging*, vol. 5, pp. 301–316, June 2019.

[4] Imec, "Real-time hyperspectral snapshot cameras." https://www.imechyperspectral.com/en/real-time-hyperspectral-snapshot-cameras, Last accessed: 2022-06-24.

[5] B. Geelen, C. Blanch, P. Gonzalez, N. Tack, and A. Lambrechts, "A tiny VIS-NIR snapshot multispectral camera," in *Advanced Fabrication Technologies for Micro/Nano Optics and Photonics VIII* (G. von Freymann, W. V. Schoenfeld, R. C. Rumpf, and H. Helvajian, eds.), SPIE, Mar. 2015.

[6] G. R. Arce, D. J. Brady, L. Carin, H. Arguello, and D. S. Kittle, "Compressive coded aperture spectral imaging: An introduction," *IEEE Signal Process. Mag.*, vol. 31, no. 1, pp. 105–115, 2013.

[7] J. Brauers and T. Aach, "A color filter array based multispectral camera," in *12. Workshop Farbbildverarbeitung* (G. C. Group, ed.), (Ilmenau), October 5-6 2006.

[8] L. Miao, H. Qi, R. Ramanath, and W. Snyder, "Binary tree-based generic demosaicking algorithm for multispectral filter arrays," *IEEE Trans. Image Process.*, vol. 15, pp. 3550–3558, Nov. 2006.

[9] J. Mizutani, S. S. Ogawa, K. Shinoda, M. Hasegawa, and S. Kato, "Multispectral demosaicking algorithm based on inter-channel correlation," in *Proc. IEEE VCIP'14*, pp. 474–477, 2014.

[10] S. Mihoubi, O. Losson, B. Mathon, and L. Macaire, "Multispectral demosaicing using pseudo-panchromatic image," *IEEE Trans. Comput. Imaging*, vol. 3, pp. 982–995, Dec. 2017.

[11] L. Bian, Y. Wang, and J. Zhang, "Generalized MSFA engineering with structural and adaptive nonlocal demosaicing," *IEEE Trans. Image Process.*, vol. 30, pp. 7867–7877, 2021.

[12] K. Dijkstra, J. van de Loosdrecht, L. R. B. Schomaker, and M. A. Wiering, "Hyperspectral demosaicking and crosstalk correction using deep learning," *Machine Vision and Applications*, vol. 30, pp. 1–21, July 2018.

[13] T. A. Habtegebrial, G. Reis, and D. Stricker, "Deep convolutional networks for snapshot hypercpectral demosaicking," in *Proc. IEEE WHISPERS'19*, Sept. 2019.

[14] Z. Pan, B. Li, H. Cheng, and Y. Bao, "Joint demosaicking and denoising for CFA and MSFA images using a mosaic-adaptive dense residual network," in *Computer Vision – ECCV 2020 Workshops*, pp. 647–664, Springer International Publishing, 2020.

[15] K. Feng, Y. Zhao, J. C.-W. Chan, S. Kong, X. Zhang, and B. Wang, "Mosaic convolution-attention network for demosaicing multispectral filter array images," *IEEE Trans. Comput. Imaging*, vol. 7, pp. 864–878, 2021.

[16] T. Zhang, Z. Liang, and Y. Fu, "Joint spatial-spectral pattern optimization and hyperspectral image reconstruction," *IEEE J. Sel. Topics Signal Process.*, vol. 16, no. 4, pp. 636–648, 2022.

[17] P. Li, M. Ebner, P. Noonan, C. Horgan, A. Bahl, S. Ourselin, J. Shapey, and T. Vercauteren, "Deep learning approach for hyperspectral image demosaicking, spectral correction and high-resolution RGB reconstruction," *Computer Methods in Biomechanics and Biomedical Engineering: Imaging & Visualization*, vol. 10, no. 4, pp. 409–417, 2022.

[18] J. M. Bioucas-Dias, A. Plaza, N. Dobigeon, M. Parente, Q. Du, P. Gader, and J. Chanussot, "Hyperspectral unmixing overview: Geometrical, statistical, and sparse regression-based approaches," *IEEE J. Sel. Topics Appl. Earth Observ. Remote Sens.*, vol. 5, pp. 354–379, Apr. 2012.

[19] D. D. Lee and H. S. Seung, "Learning the parts of objects by non-negative matrix factorization," *Nature*, vol. 401, pp. 788–791, Oct. 1999.

[20] Y. Deville, "Sparse component analysis: A general framework for linear and nonlinear blind source separation and mixture identification," in *Blind Source Separation*, pp. 151–196, Springer, 2014.

[21] O. Berné, C. Joblin, A. Tielens, Y. Deville, M. Puigt, R. Guidara, S. Hosseini, G. Mulas, and J. Cami, "Source separation algorithms for the analysis of hyper-spectral observations of very small interstellar dust particles," in *Proc. IEEE WHISPERS'09*, pp. 1–4, 2009.

[22] M. S. Karoui, Y. Deville, S. Hosseini, and A. Ouamri, "Blind spatial unmixing of multispectral images: New methods combining sparse component analysis, clustering and non-negativity constraints," *Pattern Recognition*, vol. 45, no. 12, pp. 4263–4278, 2012.

[23] C. Dorffer, M. Puigt, G. Delmaire, and G. Roussel, "Informed nonnegative matrix factorization methods for mobile sensor network calibration," *IEEE Trans. Signal Inf. Process. Netw.*, vol. 4, no. 4, pp. 667–682, 2018.

[24] P.-J. Lapray, X. Wang, J.-B. Thomas, and P. Gouton, "Multispectral filter arrays: Recent advances and practical implementation," *Sensors*, vol. 14, no. 11, pp. 21626–21659, 2014.

[25] F. Yasuma, T. Mitsunaga, D. Iso, and S. Nayar, "Generalized Assorted Pixel Camera: Post-Capture Control of Resolution, Dynamic Range and Spectrum," tech. rep., Nov 2008.

[26] C. Winkens, F. Sattler, V. Adams, and D. Paulus, "HyKo: A spectral dataset for scene understanding," in *Proc. IEEE ICCVW'17*, IEEE, Oct. 2017.

[27] K. Abbas, M. Puigt, G. Delmaire, and G. Roussel, "Locally-rank-one joint unmixing and demosaicing methods for snapshot spectral images. part II: a filtering-based framework." Preprint, 2023.

[28] K. Abbas, M. Puigt, G. Delmaire, and G. Roussel, "Joint unmixing and demosaicing methods for snapshot spectral images," in *Proc. IEEE ICASSP'23*, (Rhodes, Greece), 2023.

[29] D. Manolakis, R. Lockwood, and T. Cooley, *Hyperspectral Imaging Remote Sensing: Physics, Sensors, and Algorithms*. Cambridge University Press, 2016.

[30] L. Wang and C. Zhao, *Hyperspectral Image Processing*. Springer Berlin Heidelberg, 2015.

[31] J. G. Michael West and C. Galvan, "Commercial snapshot spectral imaging: The art of the possible." Available online at https://www.mitre.org/sites/default/files/publications/pr-18-3832-commercial-snapshot-spectral-imaging-art-of-possible.pdf. Last access: 08/26/2022., 2018.

[32] B. Geelen, N. Tack, and A. Lambrechts, "A compact snapshot multispectral imager with a monolithically integrated per-pixel filter mosaic," in *Advanced Fabrication Technologies for Micro/Nano Optics and Photonics VII* (G. von Freymann, W. V. Schoenfeld, and R. C. Rumpf, eds.), SPIE, Mar. 2014.

[33] IMEC, "Hyperspectral sensors user manual." Available online at Support Portal of imec https://www.imec-int.com/, 2019.

[34] B. Geelen, N. Tack, and A. Lambrechts, "A snapshot multispectral imager with integrated tiled filters and optical duplication," in *Advanced Fabrication Technologies for Micro/Nano Optics and Photonics VI* (G. von Freymann, W. V. Schoenfeld, and R. C. Rumpf, eds.), vol. 8613, p. 861314, International Society for Optics and Photonics, SPIE, 2013.

[35] B. Geelen, N. Tack, and A. Lambrechts, "A snapshot multispectral imager with integrated tiled filters and optical duplication," in *SPIE Proceedings* (G. von Freymann, W. V. Schoenfeld, and R. C. Rumpf, eds.), SPIE, Mar. 2013.

[36] L. Wang, Y. Feng, Y. Gao, Z. Wang, and M. He, "Compressed sensing reconstruction of hyperspectral images based on spectral unmixing," *IEEE Journal of Selected Topics in Applied Earth Observations and Remote Sensing*, vol. 11, no. 4, pp. 1266–1284, 2018.

[37] E. Vargas, H. Arguello, and J.-Y. Tourneret, "Spectral image fusion from compressive measurements using spectral unmixing and a sparse representation of abundance maps," *IEEE Transactions on Geoscience and Remote Sensing*, vol. 57, no. 7, pp. 5043–5053, 2019.

[38] V. Rathi and P. Goyal, "Convolution filter based efficient multispectral image demosaicking for compact msfas.," in *VISIGRAPP (4: VISAPP)*, pp. 112–121, 2021.

[39] V. Rathi and P. Goyal, “Generic multispectral demosaicking using spectral correlation between spectral bands and pseudo-panchromatic image,” *Signal Processing: Image Communication*, vol. 110, p. 116893, 2023.

[40] M. Gupta, V. Rathi, and P. Goyal, “Adaptive and progressive multispectral image demosaicking,” *IEEE Transactions on Computational Imaging*, vol. 8, pp. 69–80, 2022.

[41] X. Zhang, G. Zhang, and B. Hu, “A generic multispectral demosaicking method based on inter-channel spectrum correlation,” in *Third International Computing Imaging Conference (CITA 2023)*, vol. 12921, pp. 293–299, SPIE, 2023.

[42] X.-R. Feng, H.-C. Li, R. Wang, Q. Du, X. Jia, and A. J. Plaza, “Hyperspectral unmixing based on nonnegative matrix factorization: A comprehensive review,” 2022.

[43] J. Li and J. M. Bioucas-Dias, “Minimum volume simplex analysis: A fast algorithm to unmix hyperspectral data,” in *Proc. IEEE IGARSS 2008*, vol. 3, pp. III – 250–III – 253, 2008.

[44] T.-H. Chan, C.-Y. Chi, Y.-M. Huang, and W.-K. Ma, “A convex analysis-based minimum-volume enclosing simplex algorithm for hyperspectral unmixing,” *IEEE Trans. Signal Process.*, vol. 57, no. 11, pp. 4418–4432, 2009.

[45] A. Ambikapathi, T.-H. Chan, W.-K. Ma, and C.-Y. Chi, “Chance-constrained robust minimum-volume enclosing simplex algorithm for hyperspectral unmixing,” *IEEE Trans. Geosci. Remote Sens.*, vol. 49, no. 11, pp. 4194–4209, 2011.

[46] A. Boulais, O. Berné, G. Faury, and Y. Deville, “Unmixing methods based on nonnegativity and weakly mixed pixels for astronomical hyperspectral datasets,” *Astronomy & Astrophysics*, vol. 647, p. A105, mar 2021.

[47] F. Movahedi Naini, G. Hosein Mohimani, M. Babaie-Zadeh, and C. Jutten, “Estimating the mixing matrix in sparse component analysis (sca) based on partial k-dimensional subspace clustering,” *Neurocomputing*, vol. 71, no. 10, pp. 2330–2343, 2008.

[48] S. Zhang, J. Li, H.-C. Li, C. Deng, and A. Plaza, “Spectral–spatial weighted sparse regression for hyperspectral image unmixing,” *IEEE Trans. Geosci. Remote Sens.*, vol. 56, no. 6, pp. 3265–3276, 2018.

[49] H. Li, R. Feng, L. Wang, Y. Zhong, and L. Zhang, “Superpixel-based reweighted low-rank and total variation sparse unmixing for hyperspectral remote sensing imagery,” *IEEE Trans. Geosci. Remote Sens.*, vol. 59, no. 1, pp. 629–647, 2021.

[50] L. Qi, J. Li, Y. Wang, Y. Huang, and X. Gao, “Spectral–spatial-weighted multiview collaborative sparse unmixing for hyperspectral images,” *IEEE Trans. Geosci. Remote Sens.*, vol. 58, no. 12, pp. 8766–8779, 2020.

[51] T. Ince, “Superpixel-based graph laplacian regularization for sparse hyperspectral unmixing,” *IEEE Geosci. Remote Sens. Lett.*, vol. 19, pp. 1–5, 2022.

[52] B. Palsson, J. R. Sveinsson, and M. O. Ulfarsson, “Blind hyperspectral unmixing using autoencoders: A critical comparison,” *IEEE J. Sel. Topics Appl. Earth Observ. Remote Sens.*, vol. 15, pp. 1340–1372, 2022.

[53] J. R. Patel, M. V. Joshi, and J. S. Bhatt, “Spectral unmixing using autoencoder with spatial and spectral regularizations,” in *Proc. IEEE IGARSS’21*, pp. 3321–3324, 2021.

[54] B. Palsson, J. Sigurdsson, J. R. Sveinsson, and M. O. Ulfarsson, “Hyperspectral unmixing using a neural network autoencoder,” *IEEE Access*, vol. 6, pp. 25646–25656, 2018.

[55] J. M. Nascimento and J. M. Dias, “Does independent component analysis play a role in unmixing hyperspectral data?,” *IEEE Trans. Geosci. Remote Sens.*, vol. 43, no. 1, pp. 175–187, 2005.

[56] D. Benachir, S. Hosseini, Y. Deville, M. S. Karoui, and A. Hameurlain, “Modified independent component analysis for initializing non-negative matrix factorization: An approach to hyperspectral image unmixing,” in *Proc. IEEE ECMSM’13*, pp. 1–6, IEEE, 2013.

[57] X. Lv, W. Wang, and H. Liu, “Cluster-wise weighted nmf for hyperspectral images unmixing with imbalanced data,” *Remote Sensing*, vol. 13, no. 2, 2021.

[58] X. Lu, L. Dong, and Y. Yuan, “Subspace clustering constrained sparse nmf for hyperspectral unmixing,” *IEEE Trans. Geosci. Remote Sens.*, vol. 58, no. 5, pp. 3007–3019, 2020.

[59] C. Li, X. Chen, and Y. Jiang, “On diverse noises in hyperspectral unmixing,” *IEEE Trans. Geosci. Remote Sens.*, vol. 53, no. 10, pp. 5388–5402, 2015.

[60] R. Rajabi and H. Ghassemian, “Spectral unmixing of hyperspectral imagery using multilayer NMF,” *IEEE Geosci. Remote Sens. Lett.*, vol. 12, pp. 38–42, jan 2015.

[61] H. Fang, A. Li, H. Xu, and T. Wang, “Sparsity-constrained deep nonnegative matrix factorization for hyperspectral unmixing,” *IEEE Geosci. Remote Sens. Lett.*, vol. 15, no. 7, pp. 1105–1109, 2018.

[62] F. Xiong, Y. Qian, J. Zhou, and Y. Y. Tang, “Hyperspectral unmixing via total variation regularized nonnegative tensor factorization,” *IEEE Trans. Geosci. Remote Sens.*, vol. 57, no. 4, pp. 2341–2357, 2019.

[63] N. Yokoya, J. Chanussot, and A. Iwasaki, “Nonlinear unmixing of hyperspectral data using semi-nonnegative matrix factorization,” *IEEE Trans. Geosci. Remote Sens.*, vol. 52, no. 2, pp. 1430–1437, 2013.

[64] X. Li, J. Cui, and L. Zhao, “Blind nonlinear hyperspectral unmixing based on constrained kernel nonnegative matrix factorization,” *Signal, Image and Video Processing*, vol. 8, pp. 1555–1567, Oct. 2012.

[65] F. Zhu and P. Honeine, “Biobjective nonnegative matrix factorization: Linear versus kernel-based models,” *IEEE Transactions on Geoscience and Remote Sensing*, vol. 54, pp. 4012–4022, July 2016.

[66] S. S. Vijayashekhar and J. S. Bhatt, “A blind spectral unmixing in wavelet domain,” *IEEE J. Sel. Topics Appl. Earth Observ. Remote Sens.*, vol. 14, pp. 10287–10302, 2021.

[67] I. Meganem, P. Déliot, X. Briottet, Y. Deville, and S. Hosseini, “Linear–quadratic mixing model for reflectances in urban environments,” *IEEE Trans. Geosci. Remote Sens.*, vol. 52, no. 1, pp. 544–558, 2013.

[68] I. Meganem, Y. Deville, S. Hosseini, P. Deliot, and X. Briottet, “Linear-quadratic blind source separation using nmf to unmix urban hyperspectral images,” *IEEE Trans. Signal Process.*, vol. 62, no. 7, pp. 1822–1833, 2014.

[69] B. Yang, B. Wang, and Z. Wu, “Unsupervised nonlinear hyperspectral unmixing based on bilinear mixture models via geometric projection and constrained nonnegative matrix factorization,” *Remote Sensing*, vol. 10, no. 5, p. 801, 2018.

[70] R. A. Borsoi, T. Imbiriba, J. C. M. Bermudez, C. Richard, J. Chanussot, L. Drumetz, J.-Y. Tourneret, A. Zare, and C. Jutten, “Spectral variability in hyperspectral data unmixing: A comprehensive review,” *IEEE Trans. Geosci. Remote Sens.*, vol. 9, no. 4, pp. 223–270, 2021.

[71] G. Zhang, S. Mei, B. Xie, M. Ma, Y. Zhang, Y. Feng, and Q. Du, “Spectral variability augmented sparse unmixing of hyperspectral images,” *IEEE Transactions on Geoscience and Remote Sensing*, vol. 60, pp. 1–13, 2022.

[72] H. Liu, Y. Lu, Z. Wu, Q. Du, J. Chanussot, and Z. Wei, “Spectral variability bayesian unmixing for hyperspectral sequence in wavelet domain,” *IEEE Transactions on Geoscience and Remote Sensing*, 2023.

[73] C. Dorffer, M. Puigt, G. Delmaire, and G. Roussel, “Fast nonnegative matrix factorization and completion using Nesterov iterations,” in *Proc. LVA/ICA’17*, vol. 10169 of *LNCS*, pp. 26–35, Feb. 2017.

[74] N.-D. Ho, *Non negative matrix factorization algorithms and applications*. Phd thesis, Université Catholique de Louvain, 2008.

[75] S. Zhang, W. Wang, J. Ford, and F. Makedon, “Learning from incomplete ratings using non-negative matrix factorization,” in *Proc. SIAM ICDM’06*, pp. 549–553, SIAM, 2006.

[76] N. Guan, D. Tao, Z. Luo, and B. Yuan, “NeNMF: An optimal gradient method for nonnegative matrix factorization,” *IEEE Trans. Signal Process.*, vol. 60, pp. 2882–2898, June 2012.

[77] D. Arthur and S. Vassilvitskii, “K-means++: The advantages of careful seeding,” in *Proc. SODA’07*, p. 1027–1035, SIAM, 2007.

[78] M. Puigt and Y. Deville, “Iterative-shift cluster-based time-frequency BSS for fractional-time-delay mixtures,” in *Proc. ICA’09*, pp. 306–313, 2009.

[79] J. M. P. Nascimento and J. M. Bioucas-Dias, “Vertex component analysis: a fast algorithm to unmix hyperspectral data,” *IEEE Trans. Geosci. Remote Sens.*, vol. 43, no. 4, pp. 898–910, 2005.

[80] N. Gillis and S. A. Vavasis, “Fast and robust recursive algorithmsfor separable nonnegative matrix factorization,” *IEEE Trans. Pattern Anal. Mach. Intell.*, vol. 36, no. 4, pp. 698–714, 2014.

[81] “U.S. Geological Survey (USGS) spectral library.” https://www.usgs.gov/labs/spectroscopy-lab/science/spectral-library, Last accessed: 2022-10-24.